Seismic noise interferometry and Distributed Acoustic Sensing (DAS): measuring the firn layer S-velocity structure on Rutford Ice Stream, Antarctica

Wen Zhou[1], Antony Butcher[1], Alex Brisbourne[2], Sofia-Katerina Kufner[2], J-Michael Kendall[3], Anna Stork[4]

[1]University of Bristol, BS8 1TH, Bristol, UK

[2]British Antarctic Survey, CB3 0ET, Cambridge, UK

[3]University of Oxford, OX1 2JD, Oxford, UK

[4]Silixa, WD6 3SN, Borehamwood, UK

Corresponding author: Wen Zhou (wz18709@bristol.ac.uk)

Key Points:

- DAS is used for the first time to image the S-wave velocity structure and anisotropy of the firn layer in Antarctica.
- DAS seismic interferograms are greatly improved through selective stacking and cross-correlation with a geophone.
- Our method is suitable for large-scale measurements and is feasible in the presence of ice lenses where refraction methods are inadequate.

Abstract

Firn densification profiles are an important parameter for ice-sheet mass balance and palaeoclimate studies. One conventional method of investigating firn profiles is using seismic refraction surveys, but these are limited to point measurements. Distributed acoustic sensing (DAS) presents an opportunity for large-scale seismic measurements of firn with dense spatial sampling and easy deployment, especially when seismic noise is used. We study the feasibility of seismic noise interferometry on DAS data for characterizing the firn layer at the Rutford Ice Stream, West Antarctica. Dominant seismic energy appears to come from anthropogenic noise and shear-margin crevasses. The DAS cross-correlation interferometry yields a noisy Green's function (Rayleigh waves). To overcome this, we present two strategies for cross-correlations: (1) hybrid instruments – correlating a geophone with DAS, and (2) selected stacking where the cross-correlation panels are picked in the tau-p domain. These approaches are validated with results derived from an active survey. Using the retrieved Rayleigh wave dispersion curve, we inverted for a high-resolution 1D S-wave velocity profile down to a depth of 100 m. The inversion spontaneously retrieves a 'kink' (velocity gradient inflection) at ~12 m depth, resulting from a change of compaction mechanism. A triangular DAS array is used to investigate directional variation in velocity, which shows no evident variations thus suggesting a lack of deformation in the firn. Our results demonstrate the potential of using DAS and seismic noise interferometry to image the near-surface and present a new approach to derive S-velocity profiles from surface wave inversion in firn studies.

Plain Language Summary

The density distribution (density versus depth) of tens of meters at the top of a glacier is an important feature of ice-sheet mass balance and palaeoclimate research. It can be estimated using

the empirical relationship between density and seismic P-wave velocity. The P-wave velocity can be measured using a seismic refraction survey with geophones and active sources. However, refraction seismic surveys are expensive for measurements over large areas. Distributed Acoustic Sensing (DAS) using fibre optic cables to detect seismic waves is an emerging dense spatial sampling seismic acquisition technology. It can be used in conjunction with seismic noise cross-correlation to make large-scale measurements easier and cheaper than with conventional geophones. We investigate the feasibility of this approach on Rutford Ice Stream, West Antarctica, and propose two approaches to improve DAS seismic-noise cross-correlation results. Surface waves are retrieved by seismic noise cross-correlation and are used to estimate the S-wave velocity structure. Our S-velocity profile resembles an independently measured P-velocity in-shape and spontaneously retrieved a velocity gradient inflection—related to changes in the ice compaction mechanism. We show that DAS and seismic noise interferometry can be used for future firn measurements, but also more generally in studies of the near-surface.

1 Introduction

Firn is partially compacted granular snow, the intermediate stage between fresh snow and the underlying glacial ice. It has a depth-increasing density resulting from burial by subsequent accumulation the overburdened weight compacts the snow and reduces porosity by grain packing, deformation, and sintering (Alley, 1987; Cuffey & Paterson, 2010).The depth-density profile is controlled primarily by the temperature and snow accumulation rate and is highly variable due to the broad range of climatic conditions across the Antarctica continent (e.g., van den Broeke, 2008). Knowledge of the firn layer is crucial for improving altimetric mass-balance estimates (Shepherd et al., 2012) and palaeoclimate reconstructions (Craig et al., 1988). Additionally, studying the firn layer properties may help to constrain models of surface melt leading to ice shelf retreat (van den Broeke, 2005). However, such as shear deformation along ice stream shear-margin (Riverman et al. 2019) and glacier dynamics (Hollmann et al., 2021) also influence firn structures, which suggests a comprehensive study of the Antarctica firn may be required to improve ice-sheet mass balance estimates.

Conventionally, the structure and densification profile of firn is directly measured from ice core or borehole logging (e.g. Morris et al., 2017), or indirectly using for example seismic P-wave refraction (e.g. Kirchner & Bentley, 1979) or radar measurements (e.g., Case & Kingslake, 2022). A specific version of seismic refraction inversion was developed for the investigation of firn structures by Kirchner & Bentley (1979). The method uses curve fitting with a double-exponential form applied to diving wave travel times, prior to a Wiechert-Herglotz-Bateman (WHB) velocity-depth inversion (Slichter, 1932). These results are commonly used to correct seismic reflection surveys for near-surface effects (e.g., Peters et al., 2006; Smith, 1997), derive elastic properties of firn (King & Jarvis, 2007; Schlegel et al., 2019), and investigate its spatial variations and azimuthal anisotropy.

The presence of anisotropy in the firn layer has been reported previously. Kirchner & Bentley (1990) indicate substantial azimuthal anisotropy in the upper 30-40 m and state that simple transverse isotropy with a vertical symmetry axis (VTI) expected from firn compaction is not always appropriate. A recent study by Hollman et al. (2021) infers seismic anisotropy in the firn on the Amery Ice Shelf in the proximity of former shear margins. Polarimetric radar measurements have also indicated the presence of complex near-surface anisotropy on both Whillans and Rutford Ice Streams (Jordan et al, 2020; Jordan et al., 2022), in general related to ice flow and surface strain rates.

Although the WHB method is viable for both P- and S-wave velocity measurement, the former is by far the most widely used due to the greater ease of generation and identification of P-wave energy. However, King & Jarvis (2017) observed a variation of Poisson ratio with depth in the firn layer, suggesting that measuring S-wave velocity is important for studying firn elasticity and densification.

In addition, because a commonly used WHB refraction inversion method fits a double exponential velocity profile to the travel-time data, it can only apply to a typical compacted firn with monotonically increasing seismic velocity over depth and with one ‘kink’ (critical density) from a change of compaction mechanism and without any ice lenses (Kirchner & Bentley, 1979).

Furthermore, with conventional geophone sensors, it is time-consuming and more expensive to apply the refraction survey to cover a large area, because of the dense receiver spacing at the near offset required by the WHB inversion. Thus, most previous refraction surveys are limited to effectively -point measurements with a scale of a few hundred meters (Hollmann et al., 2021; King & Jarvis, 2007; Schlegel et al., 2019). Recently, Riverman et al (2019) conducted a 40 km refraction survey but with a sparse geophone spacing of 20 m which showed a poor resolution in the upper ~20 m of the firn.

Therefore, any new seismic technique capable of measuring S-wave velocities, measuring firn layer anomalies including ice lenses or low-velocity zones, or with better scaling capabilities, would be beneficial for future studies of firn. In this study, we investigate the feasibility of using DAS data, seismic noise interferometry, and surface (Rayleigh) wave inversion to address the aforementioned problem by performing distributed acoustic sensing (DAS) measurements on Rutford Ice Stream, West Antarctica.

In recent years, there has been a rapid development of DAS in seismic acquisition. DAS is an optical fibre sensing technology that offers the potential of broadband frequency recording and near-continuous spatial sampling of earth strain and temperature variation signals (Ajo-Franklin et al., 2019; Ide et al., 2021). Its unprecedented spatial sampling could improve the spatial resolution of subsurface seismic images (Ajo-Franklin et al., 2019; Dou et al., 2017; Lellouch et al., 2019; Rodríguez Tribaldos et al., 2019; Rodríguez Tribaldos & Ajo-Franklin, 2021; Spica, Nishida, et al., 2020; Williams et al., 2019).The sensing element of DAS is the optical fibre without electronic or mechanical components, which makes the technology an attractive option for long-term, low-maintenance deployments for glacial studies (Booth et al., 2020; Brisbourne et al., 2021; Hudson et al., 2021; Walter et al., 2020), for in-situ measurement in deep boreholes for active fault (Lellouch et al., 2019), geothermal, hydrocarbon storage (Correa et al., 2018; Mateeva et al., 2017) or hydrogen storage monitoring, and for submarine environments (Lior, Sladen, et al., 2021; Spica, Nishida, et al., 2020; Williams et al., 2019). It could also be suitable for critical infrastructure (e.g. nuclear plants; Butcher et al. (2021), dams, embankments, etc).

Seismic noise interferometry is a simple and convenient method, from both data processing and acquisition perspectives. Many studies have used the method to retrieve surface waves for studying ice-sheets. For example, using broadband seismometers, Walter et al. (2015) used surface wave energy from crevasse events to derive the Rayleigh wave response between stations. Sergeant et al. (2020) retrieved Rayleigh waves between stations at a number of sites in Greenland and the Alps using a range of noise sources. Also, in the Alps at Glacier de la Plaine Morte, Switzerland, measurements of azimuthal variation in Rayleigh wave velocity indicate that crevasses cause up to 8% anisotropy (Lindner et al., 2019). Chaput et al. (2022) investigated noise interferometry and H/V for characterising the firn layer in West Antarctica. DAS has recently been used in glacier settings for noise interferometry by Walter et al. (2020), who retrieved Rayleigh wave (above 10 Hz) from cross-correlations. However, to the best of our knowledge, no study has provided a complete S velocity profile for the glacier firn layer, which is potentially an important constraint for firn densification models.

It can be challenging to apply noise interferometry on DAS, especially in low ambient noise environments. Compared with conventional seismometers or geophones, DAS has higher instrument self-noise (e.g., optical system noise) which can obscure the weak seismic 'noise' that is the crucial 'signal' for noise interferometry. Nevertheless, in recent years, there have been successful applications of DAS for ambient surface wave imaging in submarine environments, using microseism noise at 0.6 – 1 Hz (Spica, Nishida, et al., 2020), 0.5 – 5 Hz (Cheng et al., 2021) and 1 – 3 Hz (Lior, Mercerat, et al., 2021). The advantage of recording in the offshore environment is the stable seafloor temperature and shorter distance to microseism noise sources. Onshore applications have been also successful (e.g., Dou et al., 2017; Rodríguez Tribaldos & Ajo-Franklin, 2021; Spica, Perton, et al., 2020), with reported applications mostly limited to urban environments with strong anthropogenic (traffic, mechanical) noises at frequencies typically above 5 Hz. However, it is still rare to apply DAS noise interferometry in remote non-urban areas onshore.

In this manuscript, firstly, we present examples of raw DAS continuous recordings, which are primarily dominated by anthropogenic noise (from a snowmobile and a petro-generator) and crevasse surface wave events. We also investigate the nature of the low-frequency (< 1 Hz) part of the recording. Secondly, we demonstrate that Rayleigh waves can be retrieved through noise interferometry using data acquired on a linear DAS cable. The interferograms can be improved with hybrid-instrumenting and selective stacking of noise cross-correlations. Thirdly, the fundamental mode Rayleigh wave dispersion curve is extracted and inverted to obtain an S-wave velocity (Vs) profile. As a verification, we compare these results with dispersion analysis of the surface waves captured by an active survey using a sledgehammer and plate source. Finally, we use the data from a triangular DAS array to investigate the seismic anisotropy of the firn.

2 Field experiment and data acquisition

Rutford Ice Stream (Figure 1a) is a fast-flowing ice stream draining part of the West Antarctic Ice Sheet into the Ronne Ice Shelf. At the experiment location, 40 km upstream of the grounding line, it is around 25 km wide and 2200 m thick, with ice flow of ~380 m a^{-1} (Murray et al., 2007).

Between 11th and 24th January 2020, an experiment was carried out at Rutford Ice Stream (Figure 1a) utilizing both DAS and geophones for passive and active surveys. The seismic arrays were collocated and installed at the centre of the ice stream where the surface is mostly flat (Figure 1a), to record the regularly occurring icequakes originating from the base of the glacier where it slides over the bed (Hudson et al., 2021; Kufner et al., 2021; Smith et al., 2015). A second aim was to image the firn layer using seismic noise and active sources. The DAS data were acquired using a Silixa iDAS v2 interrogator connected to a 1 km six channel tight buffered single mode fibre optic cable. The cable was deployed in linear and triangular configurations, successively. The iDAS measures strain rate of the optical fibre. For the passive measurement, we used a 1 kHz sampling rate, 10 m gauge length, and 1 m channel spacing. A petrol generator (Honda EU10i 1kW) was deployed as the power supply, which was located on the snow surface, 50 m away from the interrogator in a direction aligned with the orientation of the fibre (Figure 1b).

The cable was laid in the track of a snowmobile and initially deployed without burial, but subsequently buried with a layer of approximately 5 cm of snow. Hudson et al. (2021) described these data and investigated the suitability of DAS for micro-seismicity (icequakes) monitoring. Butcher, Hudson, et al. (2021) further explored the utility of DAS data using array-based processing methods. Hudson et al. (2021) also investigated the difference between buried and unburied cable. They showed that even a shallow burial of the cable made a significant difference in attenuating the unwanted noise and enhancing the lower frequency (below 1 Hz) signal. They suggested that the better coupling to the ice results in an improved sensitivity to the primary and secondary microseisms, making it useful for ambient noise tomography studies. For frequencies 1 to 70 Hz, the buried cable has a lower noise level, thanks to its better coupling and lower wind noise. Since only the seismic noise is useful for imaging the subsurface, we concentrate on the period of time when the cable was buried.

The geophone network consisted of sixteen 4.5 Hz 3-component Geospace GS-11D geophones with Reftek RT130 dataloggers with a 1 kHz sample rate. The geophone array layout was primarily designed to detect and locate icequakes (Figure 1b). Three geophones were collocated or were in-line with the fibre, and they were approximately positioned in the middle and at either end of the linear DAS array.

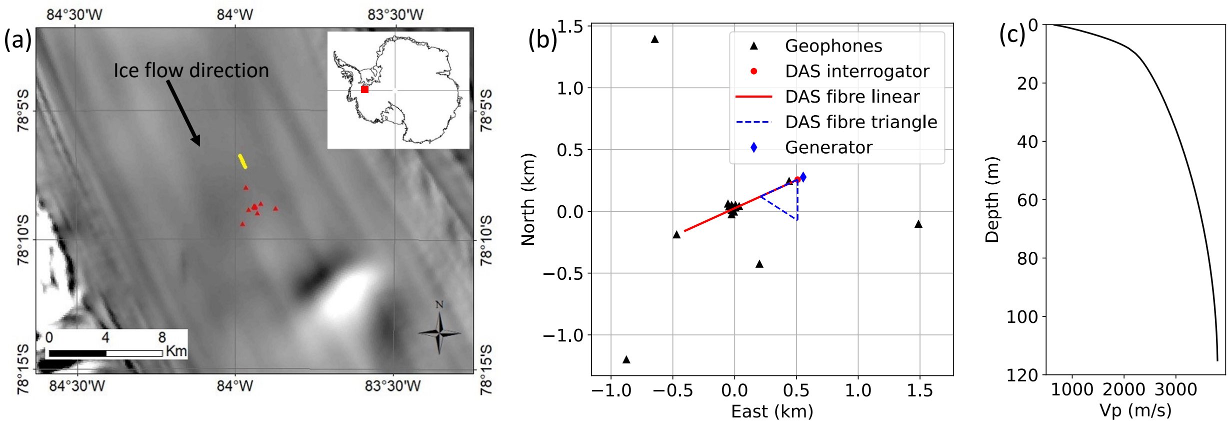

Figure 1. (a) Location of seismic experiment on Rutford Ice Stream. Geophone stations are shown as red dots. The background is Moderate-resolution Imaging Spectroradiometer (MODIS) imagery (Scambos et al., 2007). Geophones are shown as red dots. The yellow line indicates the location of a previous refraction survey (Smith et al., 2021)*. (b) The relative position (reference at the centre of the geophone array) of instruments. Geophones (black triangles) were designed for array processing. DAS fibres (red solid line and blue dashed line) were connected to the DAS interrogator at the east end. The generator (diamond) sits 50 m away from the interrogator. (c) Firn P wave velocity profile from a refraction experiment* (Smith et al., 2021)*, using an expanding interval of vertical component geophones*

In addition to the passive measurements, an active seismic survey was also acquired along the linear array using a sledgehammer (4.5 kg) and plate source. These shots were recorded by the iDAS interrogator at 8 kHz sampling rate. At the 21 source locations (every 50 m from 10 to 1000m along the fibre), a total of 42 shot-gathers were acquired, with two or four shots per location. In general, the data quality of these shot-gathers is high, with signals captured across the entire 1km linear array without the need for stacking. An example shot-gather from this survey is presented in Figure 2, which shows dominant seismic phases including refracted (diving) P-waves and Rayleigh waves, as indicated. The shot times are constrained from the onset of the DAS record (Figure 2b, the first record is the strain generated by the hammer plate impact). Due to the averaging effect of the 10 m gauge length, very near offset DAS recordings are distorted (Figure 2 b) which limits the accuracy of the near-surface Vp in a WHB refraction inversion. Research on overcoming this plateau effect is working in progress.

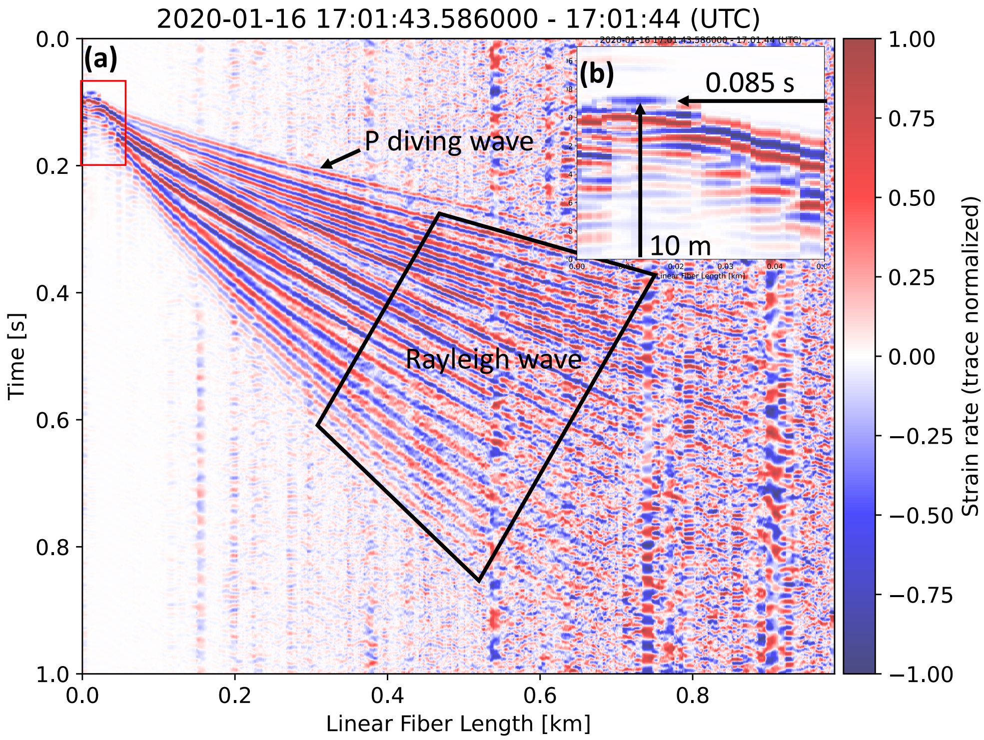

Figure 2. An example of active shot data from a hammer and plate source. (a) A shot gather on the 1 km linear fibre (1 m channel distance plotted), with the source at 10 m from one end of the fibre. The strain rate waveforms are normalized over each DAS channel. Signal is bandpass filtered 5 to 100 Hz. Note 0 s is not the trigger time, but an arbitrary stamp as shown in the figure. (b) is a zoom-in of the (a) as indicated by the red box. Around the shot location (10 m), the first arrivals are flat, which is an artefact of the 10 m gauge DAS length.

A conventional P-wave seismic refraction survey was previously acquired 2.6 km upstream of the study area (Figure1a), using a surface source and expanding spread of vertical component geophones out to a maximum offset of 980 m, as part of the site survey for the BEAMISH subglacial drilling project (Smith et al., 2021). Using this refraction dataset, we derived a P-wave velocity depth profile using the WHB based inversion method of Kirchner & Bentley (1979) (Figure 1c). With this method, Kirchner & Bentley (1990) report velocity uncertainty of ±60 m/s near the surface, reducing to ±15 m/s at 50 m depth on Ross Ice Shelf, which we assume similar in our inversion given the similarity of firn structures of the two sites.

3 DAS noise characterization on the linear array

Prior to the noise interferometry analysis, we seek to characterise the seismic noise recorded on the DAS array, as noise interferometry is a relatively new application to DAS data in a glacial setting (Walter et al., 2020).

For a conventional seismic array, seismic noise is analysed with beamforming, which estimates the apparent velocity and azimuth of the coherent wavefield, such as in Chaput et al. (2022). van den Ende & Ampuero (2021) firstly applied beamforming to DAS recorded earthquake signal using a fibre with a 2D deployment. However, performing the beamforming with a 1D array results in a symmetric ambiguity. We thus simply visualize the DAS data in the time-space (time dimension in one axial direction and channel distance in the other) plot for 4 frequency bands (<1 Hz, 1 – 10 Hz, and 10 -100 Hz). We then manually inspect the signal coherency. To improve the efficiency of this visualization process, we down sample the DAS channel distance to 10 m, and a sample rate of 200 Hz.

3.1 Anthropogenic noise (>10 Hz)

In Figure 3 we present an example of high-frequency noise (1 Hz high-pass filtered), which began abruptly at around 45 seconds and lasted to approximately 200 seconds. It was recorded on the linear array DAS, with decreasing amplitude from 0 to ~400 m along the cable (Figure 3a). We examine the frequency content of this signal by creating a spectrogram (Figure 3c) for the record at 100 m (Figure 3b), using a short-time Fourier transform. In this record, the signal starts with a varying frequency over 10 to 70 Hz from around 45 s, then settles at a constant frequency around 25 Hz, 35 Hz and 50 Hz at ~70 s. This vibration pattern repeats one more time, before the signal gradually disappears around 250 s. We speculate that this signal is from a snowmobile when we use it to approach the generator for refueling. The generator creates a constant 33.3 and 66.6 Hz signal. The generator was 50 m away from the DAS channel at 0 m, the site of the recording interrogator in a tent (Figure 1b).

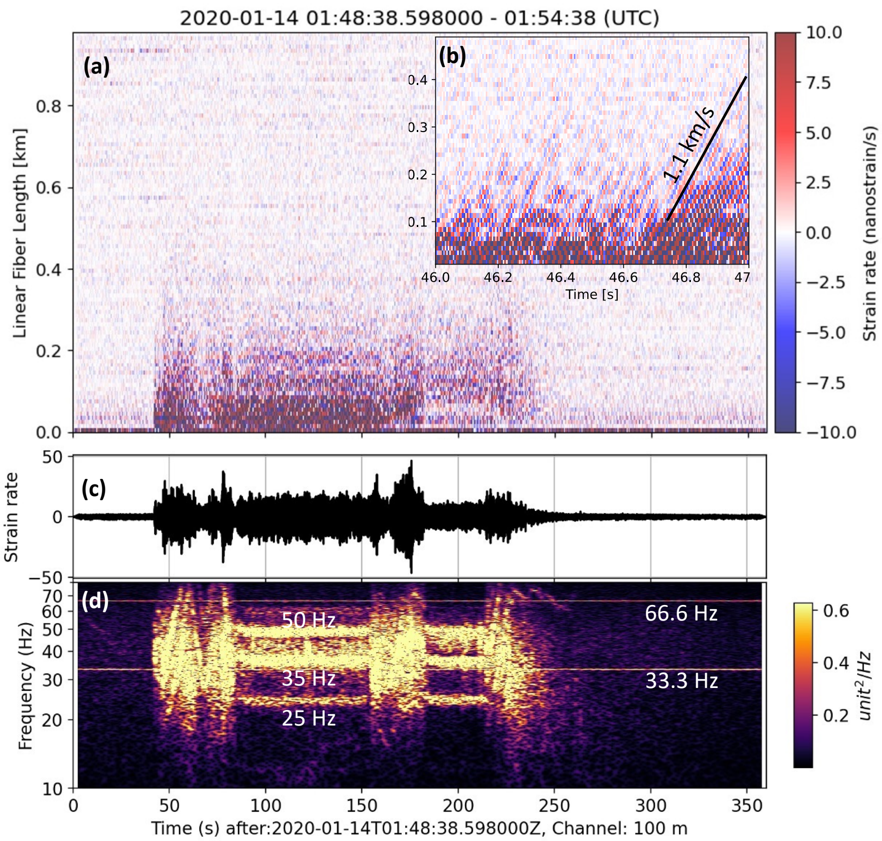

Figure 3. An example of recorded anthropogenic noise. (a) Six minutes of DAS recording after median value been subtracted for each time step, and bandpass filter 1 to 100 Hz, with amplitude represented in colour saturated between -10 and 10 nanostrain/s. (b) A zoom-in of (a) for 46-47 seconds at 0 to 500 m. (c) Time series for DAS channel at 100 m. (d) spectrogram of channel 100 m calculated from FFT with a 2-second sliding window.

3.2 Crevasse signals (1 - 10 Hz)

In the frequency band 1 to 10 Hz, we find transient surface wave events, an example of which is shown in Figure 4. In this example, the wave train is travelling approximately parallel with the fibre from 0 m to 1 km, with an apparent velocity around 1.8 km/s, close to the surface wave velocity below 10 Hz, as will be shown in Section 5 (Figure 9). But it is difficult to locate this event from the 1D DAS array. The dispersion behaviour of the signal is clearly shown in the spectrogram in Figure 4c. More than 2000 such events are detected on the 2D geophone array from one month of recording. Using differential travel-times across the geophone array calculated from cross-correlations, 248 of such events are located and reported in the supplementary information (Figure S2). They appear to originate from the shear margin of the glacier. In this manuscript, we refer to these as 'crevasse events', bearing in mind that it may not be accurate and the exact sources of these signals have not been resolved in the study, but crevasse and ice fractures at and beyond the shear margins are two potential candidates. Similar signals have contributed to ambient noise analysis at an alpine glacier (Walter et al., 2015, 2020).

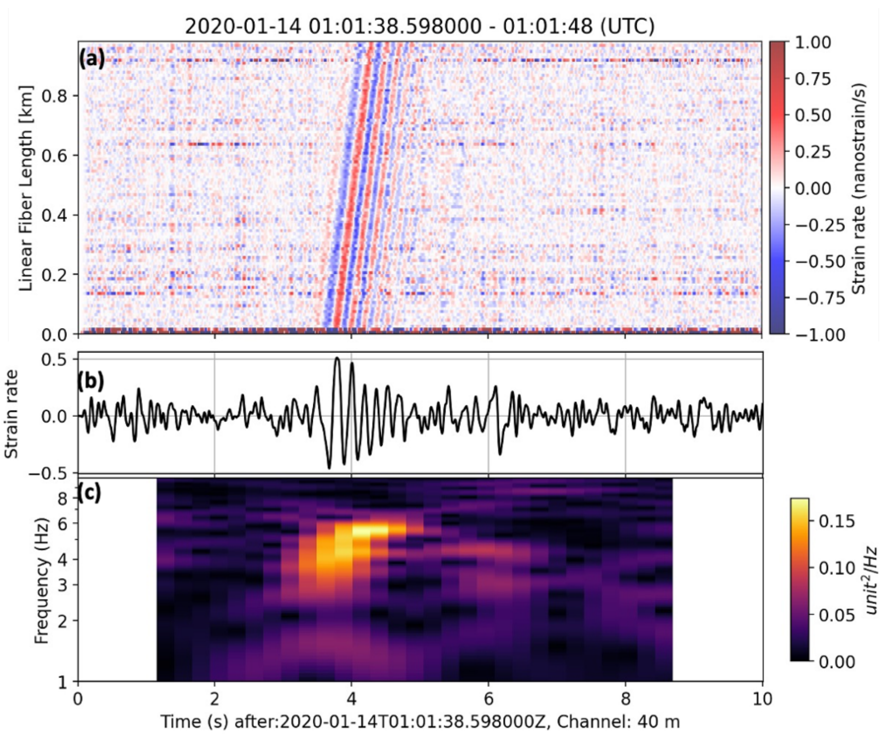

Figure 4. An example surface wave signal from a presumable crevassing event. (a) Ten seconds of DAS measurement after median removal and bandpass filter 1 to 10 Hz, with amplitude represented in colour saturated between -1 and 1 nanostrain/s. (b) Time series for the DAS channel at 40 m. (c) Spectrogram of channel 40 m calculated from FFT with a 2-second sliding window

3.3 Wind-correlated signals (< 1 Hz)

For data below 1 Hz, we find coherent signals with periods longer than 100 seconds (lower than 0.01 Hz) (Figure 5a). These signals are mostly travelling towards 0 m along the DAS cable and have propagating speeds of the order of 10 m/s, as shown in the f-k domain (Figure 5b). In the frequency band 0.1 to 1 Hz, there are signals that oscillate at 3 isolated frequencies (Figure 5d). Interestingly, when comparing amplitude in Figure 5c with frequencies in Figure 5d, there seems to be a correlation: the higher the strain rate below 0.01 Hz, the higher the oscillation frequency between 0.1 to 1 Hz (e.g., from 10000 s to 20000 s). Although the correlation does not always hold.

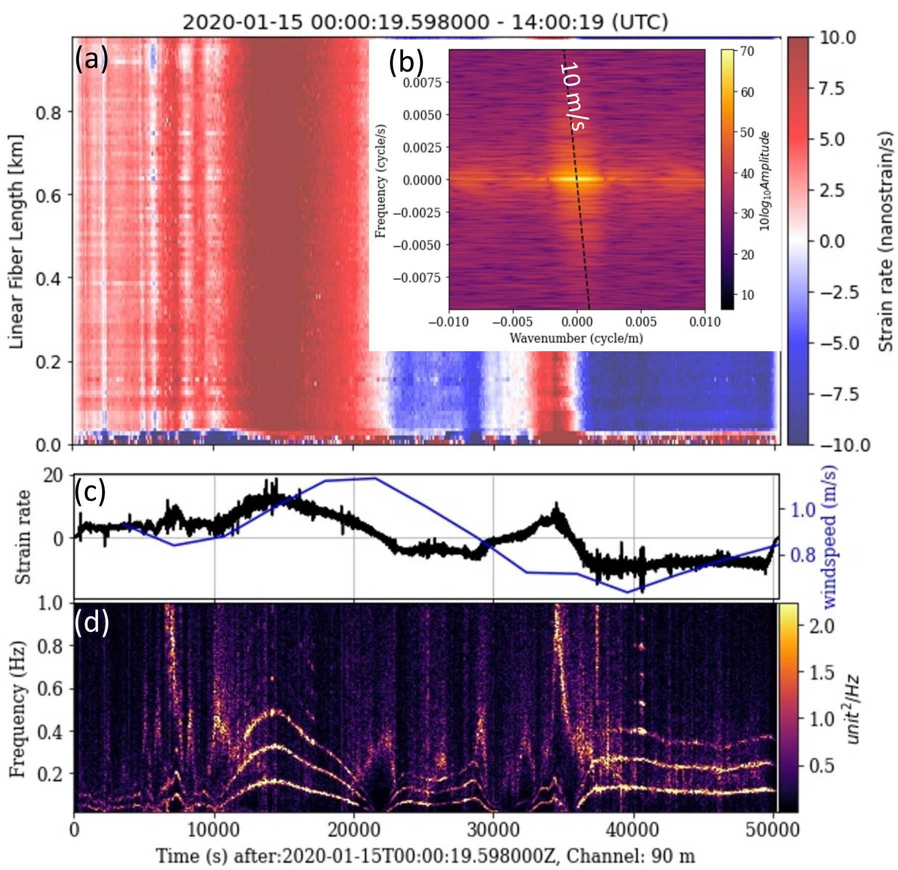

Figure 5. Low frequency signals recorded by DAS (after a 1 Hz low pass filter). (a) 14 hours DAS recording, with amplitude represented in colour saturated between -10 and 10 nanostrain/s. (b) The f-k transform of the first 10000 seconds of DAS data.

(c)The waveform at channel 120 m and predicted windspeed by the European Centre for Medium-Range Weather Forecasts (ECMWF) at location (84W 78.1S). (d) Spectrogram of channel 120 m calculated from FFT with a 100-second sliding window.

To investigate the origin of these coherent signals, we compare the waveform with the meteorological forecast model from ECMWF--European Centre for Medium-Range Weather Forecasts, (2017). We find a correlation between the 1 Hz low-passed waveform and windspeed prediction (Figure 5c), i.e., the higher the wind speed, the higher the strain rate. It might suggest that wind-induced pressure variation on the ice surface was sensed by the optical fibre. In addition, wind-induced air oscillation may be the source of the oscillating signal from 0.01 to 1 Hz. We observe that the oscillation signals from 0.01 to 1 Hz have no spatial coherence when looking at the f-k domain (Figure S1d), which might suggest they are caused by the direct impact of the wind. Additionally, in the cross-correlations (Figure 6b), we also see the strain signal of a moving marker-flag driven by the wind, although that signal is higher in frequency (9 Hz). Although these explanations are somewhat speculative, they all point to the same cause: wind. It is thus concluded that the shallow buried cable still measures mostly wind-correlated noise below 1 Hz, although it has a better coupling and a lower noise level compared with unburied cable (Hudson et al., 2021). Our observations suggest that including weather measurements such as wind speed and direction might be helpful with interpretation of future seismic acquisitions with DAS.

4 Seismic Noise Interferometry

4.1 Cross-correlation interferometry

Since the work of Shapiro et al. (2005) and Shapiro & Campillo (2004), seismic noise interferometry (SI) has become a well-established technique to probe subsurface seismic properties, especially with surface waves derived from ambient microseism noise (Bensen et al., 2007; Shapiro et al., 2005; Shapiro & Campillo, 2004). It is termed seismic noise interferometry as the method utilizes continuous seismic records without specifying their sources (location and origin time) and assuming it is random and azimuthal-isotopically distributed. An extensive literature review of the subject is provided by Snieder & Larose (2013). In this paper, we term the records as 'signals', especially when we investigate their characters. But when applying seismic interferometry, coherent seismic signals and noise are collectively referred as 'seismic noise' and we do not specifically distinguish them.

Recent studies have implemented SI with DAS data in a borehole (Lellouch et al., 2019), submarine (Cheng et al., 2021; Spica, Perton, et al., 2020), and urban environment (Ajo-Franklin et al., 2019; Dou et al., 2017; Spica, Perton, et al., 2020). Most of those studies calculate interferogram by cross-correlation (CC) with a 'virtual source' at one DAS channel and then apply stacking to enhance coherent signals. This is adopted from the workflow for processing conventional seismometers or geophones data. We also adopt this workflow, and a detailed processing flow is presented in Figure S3.

Firstly, we slice the continuous data into small segments in the time-domain, then we calculate the spectrally whitened CCs:

$$c_i(\omega) = \frac{1}{N}\sum_{n=1}^{N} \frac{r_i(\omega)s(\omega)^*}{\sqrt{\overline{r_i(\omega)^2}\ \overline{s(\omega)^2}}}, \qquad i = 1, 2, \dots m$$

For each segment *n*, we decimate the sampling rate to 200 Hz, then apply a tapered cosine. A Fourier transform is applied for each channel, so the virtual source channel and each receiver channel are represented in frequency-domain: $s(\omega)$, $r_i(\omega)$ ($m = 1000$ for the linear DAS array). Since the desired seismic noise is above 1 Hz, we choose a segment length of 10 seconds, with an overlap of 5 seconds. To keep the process simple, we do not apply time-domain normalization (1-bit) or remove the basal icequakes signals before CCs. While The power spectra, $r_i(\omega)^2$ and $s(\omega)^2$, are smoothed by a 21-sample moving average, a process known as spectral whitening. The cross-correlations over each segment $c_i(\omega)$ are stacked over every 2 minutes. These 2-minutes CCs are stored for further processing.

Although the 'CC-stacking' workflow is applied here, we note that to directly retrieve surface wave dispersion data, we could stack data in the frequency-wavenumber (f-k) domain, without calculating CC (e.g., Cheng et al., 2019; Spica, Nishida, et al., 2020). But, after f-k domain stacking, phase information is lost, and the data cannot be converted back to the time domain for inspection or further analysis.

4.2 Choice of virtual source: DAS versus geophone

DAS interferogram profiles are obtained through linearly stacking 2-minute CC panels over the entire recording period of five days (Figures 6 a & b). We produce two different interferograms. The first uses the DAS channel at 600 m as a virtual source (Figure 6a), while the second takes the vertical component of a co-located geophone, at offset ~570 m, as the virtual source (Figure 6b). In Figure 6a, we see the CCs (DAS virtual source) have the highest amplitude at 0 s delay time, which is due to coherent DAS instrument noise (Figure S1e), while the seismic responses, especially at a lower frequency and larger distance, are faint.

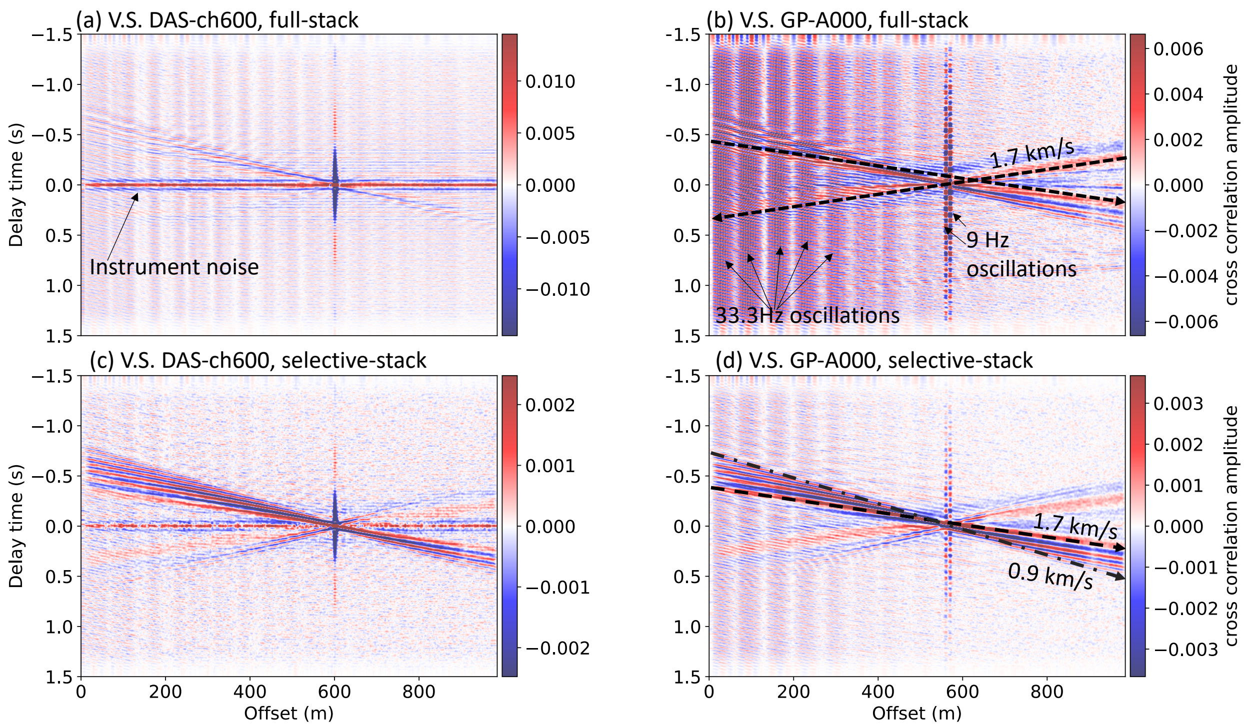

Figure 6. CCs (1 – 30 Hz, 2nd order butter bandpass zero-phase filtered) from 4 approaches. (a) Stacked cross-correlations, a virtual shot gather, with a virtual source at DAS channel at 600 m. (b) Same as (a) but with a virtual source at a geophone (A000) located close to channel 570 m. (c) Selective-stacked CCs for the same data as (a). (d) Selective-stacked CCs for the same data as (b). Note for each panel, the colour scale is saturated at the median over maximal values from each channel for visualization.

In the second approach (Figure 6b), a geophone is used as the virtual source to cross-correlate with DAS channels, which we term hybrid instrumenting CC. A clearer CC profile is retrieved, and the 0 s delay time instrument noise is completely erased. The seismic signals become clear, and we can see that they are travelling both forward (from 0 m to 1 km along the cable) and backward with an apparent velocity of ~1.7 km/s. Its dispersive nature shows that it is a surface wave. Since DAS records longitudinal strain along the fibre, parallel to the propagation direction of the retrieved signal, this surface wave is classified as a Rayleigh wave. The Rayleigh wave response between the vertical component geophone and the horizontal component DAS is the result of elliptical particle motion in the vertical plane, parallel to the direction of propagation. We have tested the process with the horizontal component (East, near parallel to the DAS cable) of the geophone, which showed little difference in terms of signal quality.

Figure 6b shows features such as the high frequency (33.3 Hz) oscillating noise that decays away from the start of the line at 0 m. This strong harmonic signal is generated by the petrol generator (Figure 3c). There is also strong 9 Hz oscillation noise around 560 and 570 m, which is likely strain produced by the wind-driven movement of the poles of two marker-flags (used to indicate the location of the geophones). Since this 9Hz noise is very localized, it does not influence further analyses.4.3 Selective stacking of cross-correlations

To improve the quality of the final interferogram image, previous studies have introduced more sophisticated techniques of stacking CCs, such as phase-weighted stacking (Schimmel et al., 2011; Schimmel & Paulssen, 1997) and SNR-weighted stacking (Cheng et al., 2015). The phase-weighted stacking suppresses incoherent noise between two CCs and has several advantages over a standard linear stack (Dou et al., 2017). This approach, however, assumes that coherent seismic noise is continuous over each time span of CCs. In our case, most of the seismic signal recorded in our dataset are transient in nature; an exception is the harmonic signal from the generator. SNR-weighted stacking is based on the SNR of CCs and has been shown to perform well for anthropogenic seismic noise above 2 Hz, which are often transient and spatially variable (Cheng et al., 2015). Manual inspection of our 2-minute CCs shows that some retrieved Rayleigh wave signals have very low SNR on individual channels. Such CCs would be down-weighted if applying SNR-weighted method. However, these weak Rayleigh wave signals are visible because of their spatial coherency, which inspired us to use spatial coherency to detect and select data containing Rayleigh wave signals.

The studies on anthropogenic noise interferometry by Zhou & Paulssen, (2020) introduced a pre-processing step by detecting and extracting noise, such as trains, for stable time-lapse CCs. That approach, however, requires a sophisticated detection scheme. Cheng et al. (2019) applied tau-p transform on processed time domain data and selected segments based on an SNR defined from the distribution of slowness (p).

Rather than selecting from the raw data, a CC-based selection scheme is computationally cheaper. Previous noise interferometry studies have selected CCs before stacking based on SNR (Olivier et al., 2015), amplitude decay (Dou et al., 2017), and apparent velocity from 2D array beamforming analysis (Vidal et al., 2014). We term these CC selection schemes as selective stacking.

For the linear DAS array, applying the linear tau-p transform (slant-stack) (Diebold & Stoffa, 1981) could highlight spatially coherent signals which have a near straight-line moveout. We thus applied tau-p transform to each 2-minute CCs panel for the frequency band 3 to 25 Hz. Following a manual inspection of the tau-p diagrams (two examples are shown in Figure 7), we find the tau-p domain maximal amplitude is a sufficient and easy to apply criteria. For CCs between geophone and DAS, we set the criteria as follows: (1) maximal amplitude is not lower than 0.0014 (CC coefficient), (2) maximum locates at delay time close to zero (0 ± 0.05 s), and with an apparent velocity smaller than 2500 m/s (slowness < -0.4 or > 0.4 s/km).

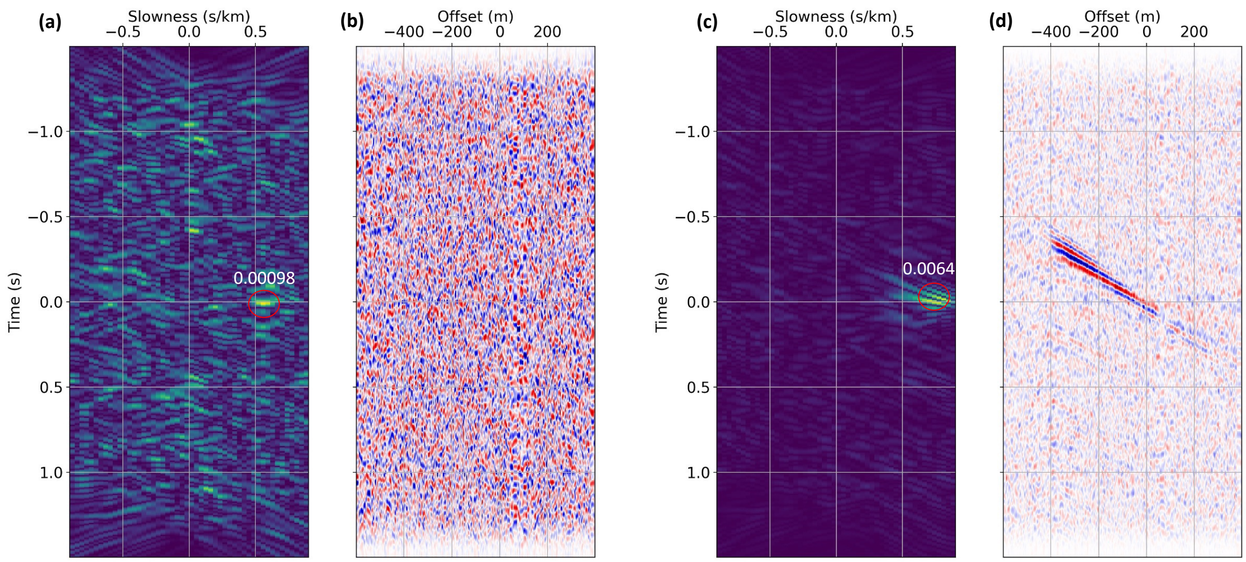

Figure 7. Examples of tau-p transform of CCs. (a, b) Example of a noisy CC panel, with peak amplitude in the tau-p domain 0.00098. (c, d) Example of a selected CC panel, with tau-p domain peak amplitude 0.0064.

These two criteria allow the selection of CCs containing clear surface wave signals. The example in Figure 7a, shows a slowness larger than 0.4 s/km and delay time close to zeros, but the maximal amplitude (0.00098) is much smaller than 0.0014, therefore this CC panel is not selected. The strong signal shown in Figure 7c meets the criteria and is therefore selected.

For the 3068 (5 days with few hours of data loss) 2-minute CC panels, 453 met the selection criterion and were linearly stacked. The selective-stacked CCs are presented in Figure 6c & d, and show much higher SNR of seismic responses compared to those for the non-selective stacked CCs (Figure 6a & b). Although for a DAS virtual source (Figure 6c), the coherent instrument noise is still present in the selectively stacked CCs, the seismic response is clearer since a large component of instrument noise is removed.

We achieve the best quality CCs for this dataset by combining a geophone as virtual source and selective stacking (Figure 6d). A signal shows clear dispersion as the higher frequency signals have a steeper slope, which indicates a slower velocity.

5 Dispersion and 1D velocity structure

5.1 Dispersion analysis

Surface wave phase velocity dispersion curves can be extracted in the frequency-velocity (f-v) domain which can be achieved with a frequency-wavenumber (f-k) transform, or through sweeping slant stack or tau-p transform for narrowly band-passed multichannel data (Xia et al., 2007). Such an approach is often termed multichannel analysis of surface waves (MASW) (Park et al., 1999; Xia et al., 1999), or PMASW for passively retrieved surface waves from CC (Cheng et al., 2016). In this study, a 2D Fourier transform (f-k transform) is applied after tapering the CCs with a Hann window in both the time and space dimensions. We further stack the positive and negative parts of the wavenumber domain to enhance the signal. These f-k diagrams (Figure S4) are then converted to the frequency– phase velocity (f-v) domain (e.g., Figure *8*a). Multiple modes of Rayleigh waves are present in both datasets, but for simplicity, only the fundamental mode dispersion curve is extracted by picking the local maximal amplitude.

For comparison, we also analysed an active dataset. Data were collected from 21 shot locations (2 or 4 shots for every 50 m) using a sledgehammer source. This survey is processed to produce a frequency-velocity plot, which is similar to that obtained from the CCs. For each shot gather, DAS channels are split into two sides by the location of the active source. The f-k transform is separately applied to both sides to avoid interference. Then, the data are stacked in the f-k domain: (1) for each f-k diagram, the negative and the positive wavenumbers are stacked. (2) for each shot gather, the two f-k diagrams are stacked. (3) for all shot gathers, they are further stacked to produce a single f-k diagram. Lastly, the f-k diagram is converted the f-v domain (Figure 8b).

The fundamental mode (Rayleigh 0) and the first higher mode (Rayleigh 1) from both the passive CCs and the active sources are shown in Figure 8. In general, there is strong agreement between the two approaches in the frequency range 15 to 50 Hz. Figure 9 shows the extracted Rayleigh 0 dispersion curves, showing a good agreement between the two approaches. This provides us with confidence that the methods adopted when producing the noise interferograms are appropriate. The passive dataset contains relatively lower frequency signals, and its dispersion curve is well constrained down to 3 Hz (Figure 8a). From Figure 8b, we see that the stacked active shots data contain signals mostly above 10 Hz with dispersion most stable between 15 and 50 Hz. This is likely due to the lack of low-frequency energy generated by the hammer and plate source, compared to ambient seismic noise. At around 33.3 Hz, there is a small but sharp reversal of velocity from the CCs derived dispersion (Figure 8a), which is due to the near-constant wavenumber of the strong noise observed at 33.3 Hz (Figure 3d and Figure 6). The strong signal causes spectral leakage in fast Fourier transforms (FFT) even though a Hann window taper was applied before the FFT. However, it does not influence our inversion as the frequency range is small.

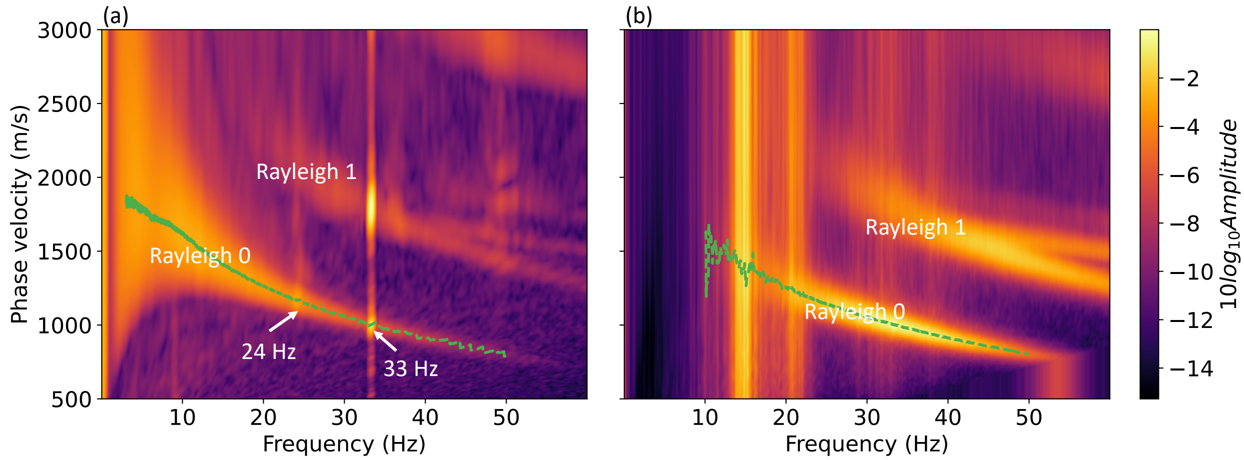

Figure 8. Extracting Rayleigh wave fundamental mode (Rayleigh 0, green dashed lines) dispersion curve from the frequency-velocity domain, by picking the local maximum amplitude. (a) Frequency-velocity plot of the stacked CCs. The Rayleigh 0 mode dispersion curve is extracted from 3 to 50 Hz. Note, that *two oscillat*ory signals are present at 24 and 33 Hz. (b) Stacked frequency-velocity plot of the 21 active shots. The Rayleigh 0 mode is extracted from 10 to 50 Hz.

5.2 Velocity inversion

Most previous surface wave inversion studies treat the subsurface as a layered model with either fixed or variable layer thickness (for two-station (Yudistira et al., 2017) or multi-station (Cheng et al., 2015; Xia et al., 1999) surveys). The firn layer is defined as a layer with continuous metamorphism of snow to ice, which results in a smooth increase of P- and S-velocity and density as a function of depth (King & Jarvis, 2007; Schlegel et al., 2019), until it becomes near constant beneath ~100 m at Rutford Ice Stream. We therefore use a near-continuous model of 100 layers, each with a layer thickness of 1 m, overlying on a half-space at the bottom of the model.

To simulate the phase velocity dispersion of the Rayleigh wave, we use the Python package disba (Luu, 2021), which was translated from the well-adapted Fortran program surf96 from Computer Programs in Seismology (Herrmann, 2013). With a 100-layer model, we significantly increase the number of variables and the non-uniqueness of the inversion. A Gaussian-Newton inversion procedure is applied using the package pyGimli (Rücker et al., 2017), with the regularization lambda to be 20, and a predefined relative error of 10% to prevent overfitting. The large relative error and regularization also means that we find a solution which is close to the starting model.

To prepare a realistic starting model, we applied the WHB inversion to the refraction data set acquired by Smith et al. (2015) to obtain a Vp model (Figure 1c). Then assuming a constant Vp/Vs=1.95 (Smith et al., 2015), we obtained a Vs model. We name this model the ‘standard Vs’ and use it as a comparison to our surface wave inverted models. The starting model for the inversion is a smoothed version of the standard Vs. The general trend of the standard Vs model is preserved but the ‘kink’ at around 9 m is smeared (Figure 10 a). Figure 10b highlights the differences between the standard Vs model and the starting model, which shows that the standard Vs model has a higher value from 0 m to ~25 m and lower value from ~25 m to 100 m.

Figure 9 shows that the starting model is generally consistent in phase velocity dispersion with that obtained from the data. At higher frequencies, the starting model has lower phase velocity than the data, which indicates the starting model underestimates the phase velocity at shallow depths.

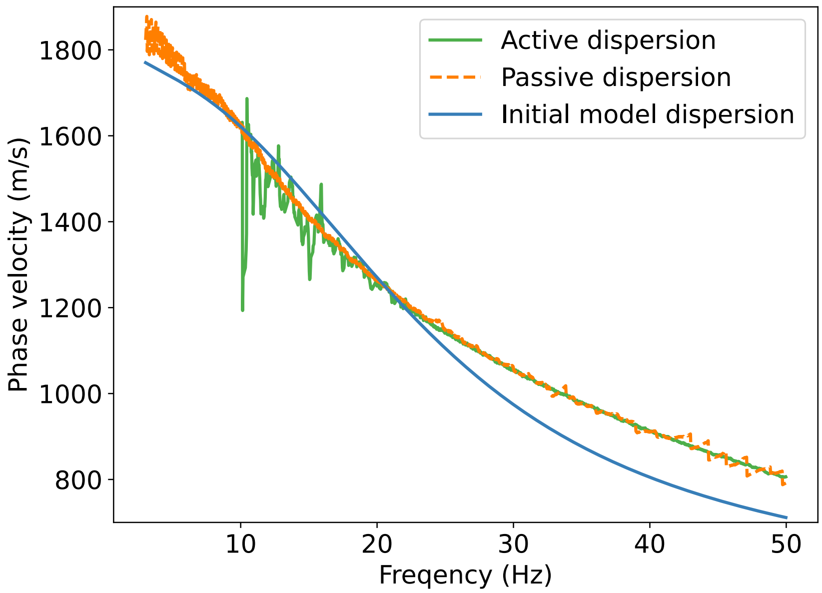

Figure 9. Comparing observed (CCs and active shots) with initial model dispersion curves, from 3 to 50 Hz. The initial Vs model is presented in Figure 10.

To capture the uncertainty in the data, we calculate the CCs for 3 geophones (1 co-located, and 2 in-line with the DAS cable). For each virtual source, we produce 9 dispersion curves, by dividing the 453 selected CCs into 9 groups for stacking. This process results in 27 (9×3) dispersion curves (Figure S5). We then invert all 27 dispersion curves for S-wave velocity profiles. Lastly, a probability density function (PDF) is calculated for each layer over its 27 measurements. The maximal point of PDFs, for each layer, represents a final Vs profile (Vs_1). In Figure 10 b, we present the inverted Vs_1 after subtracting the starting model, with the amplitudes of PDFs presented as greyscale. See Figure S3 for further details of the process.

Alternatively, Vs Figure 10is directly inverted from the dispersion curve in Figure 9 (Vs_2 in Figure 10b), which is from the fully stacked CCs (all the 453 selected time spans and 3 virtual sources).

As highlighted in Figure 10b, the Vs_1 profile is almost overlapping with the Vs_2 profile from 0 to 14 m, while the two profiles differ slight at depths below 14 m, which further indicates uncertainties of the final models. In general, our two Vs models agree with the standard Vs down to 80 m depth. Below 80 m depth, our models suggest a slightly steeper increase in velocity compared to the standard Vs, reaching up to 100 m/s higher than the initial model. In both our Vs models and the standard model, we see a clear peak (largest difference with the initial model) at around 9 m (standard Vs) to 12 m (Vs_1) depth, which is similar to the densification observation and modelled by the regional atmospheric climate model by van den Broeke (2008), across West Antarctica.

Sensitivity analysis is done at discrete frequencies (3, 6, 10, 20, 40 Hz) as shown in Figure 10c using the inverted Vs_1 model. This indicates that the highest sensitivity of most signals (> 20 Hz) is over the 0 to 40 m depth range. Signals below 10 Hz have greater sensitivity over the lower part of the model. Below 6 Hz, the Rayleigh wave is dominantly sensitive to the lowermost layer of our model, which is assumed to be a half-space.

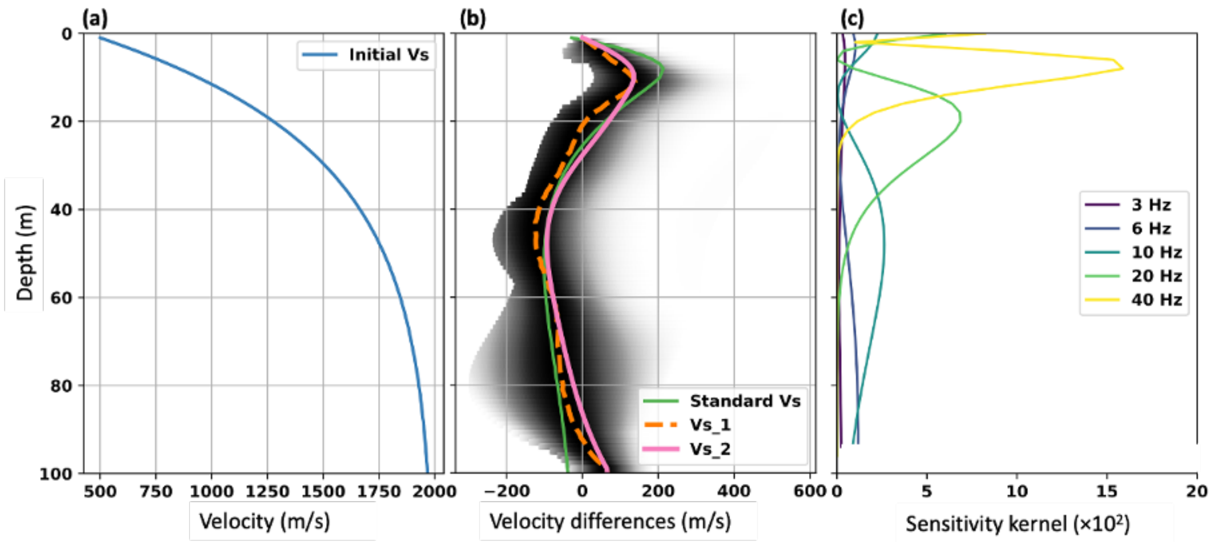

Figure 10. (a) Initial smooth Vs model. (b) Velocity difference between Inverted Vs models and the initial model, Vs_1 from maximal PDF (greyscale) and Vs_2 from direct inversion of a fully selective stacked CCs virtual shot gather. The Vs profile derived from the standard Vp refraction experiment is shown in green. (c) Sensitivity kernel calculated from the inverted model Vs_1.

5.3 Is the firn layer seismically anisotropic?

Clear azimuthal anisotropy has been reported at Rutford Ice Stream by Harland et al. (2013) and Smith et al. (2017), with the fast S-wave direction perpendicular (90°) to the ice flow direction (IFD). Hudson, Baird, et al. (2021) also observed strong shear wave splitting in icequake signals recorded by DAS. These seismic experiments do not provide constraints on the depth distribution of the anisotropic ice, as the measurements integrate over the entire wave path from the icequake hypocenter (ice-bed interface) to the surface receivers. However, using polarimetric radar measurements, Jordan et al (2022) report near-surface azimuthal anisotropy on Rutford Ice Stream, although their measurements are not coincident with this experiment.

We investigate the feasibility of imaging anisotropy with surface waves retrieved from a different azimuth on CCs. For this, we use a DAS array arranged in a triangular configuration and assume a laterally homogenous firn layer. As shown in Figure 11a, we take two segments of the triangular array (channel 50-250 and channel 670-870). We chose channels 670-870, with a larger distance to the tent and the generator, to reduce the angle between the ray path and the DAS cable. Since the snowmobile traveling from the tent to the generator is the dominant high-frequency seismic noise source, we could not retrieve a stable Rayleigh wave response from the third segment that is perpendicular to the wave propagation direction.

With virtual sources at DAS channels 150 and 750, respectively, we calculate and selectively stack CCs for each segment (Figure S6). A higher selection threshold of 0.01 is chosen as the DAS CCs are in general of higher amplitude than DAS-geophone CCs. Dispersion curves of the 2 segments are then calculated from the f-k domain (Figure S6), as with the linear-array study. In Figure 11b we show the two dispersion curves together with the result from the linear array. Note the linear array result is more stable due to the involvement of geophone data. The difference between the triangle array 90° IFD dispersion curve and the linear array result might indicate a slight horizontal heterogeneity in the firn layer. Horizontal heterogeneity might also exist between the two sides of the triangle. When comparing the two dispersion curves from the triangle array we see that they are in general nearly overlapping with each other from 10 to 27 Hz. For above 27 Hz, the 30° IFD curve indicates a slightly higher phase velocity, but the difference is small compared with the measurement uncertainties. Note that around 24 Hz and 33 Hz, there are artefacts from the f-k transform. In this study, neither the heterogeneity- nor the anisotropy-effect produces a notable dispersion curve difference between the 30° IFD and 90° IFD. Thus, it suggests that the firn layer, above ~80 m depth (for the signals above 10 Hz), is likely not strongly azimuthally anisotropic. We note that our measurements here have large uncertainty and that we cannot rule out a VTI anisotropy in the firn layer. A comparison of Rayleigh and Love wave derived shear-velocities would provide a means of testing this.

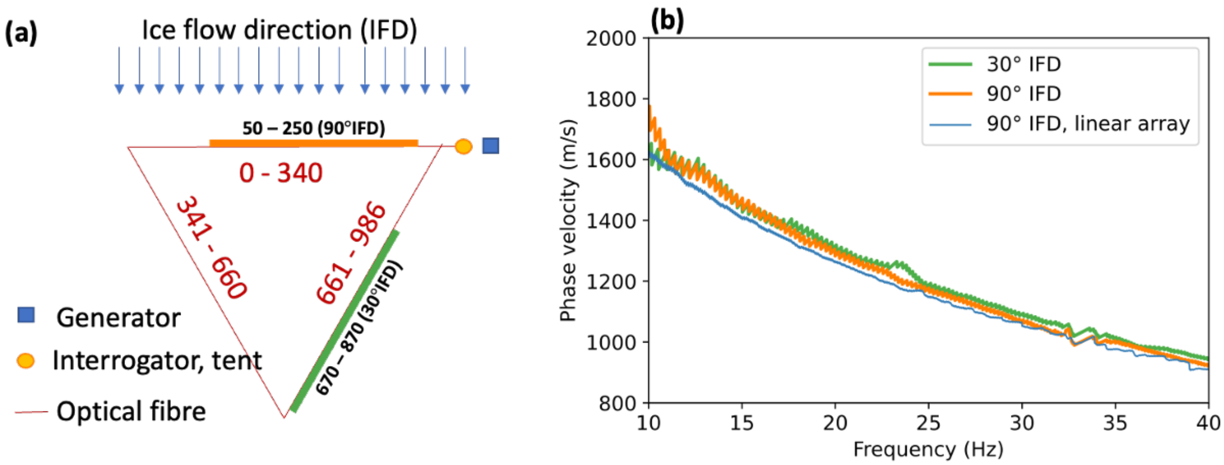

Figure 11. (a) Schematic of the geometry of the triangle DAS array, with a loop of 986 m. The thick lines indicating two 200 m DAS segments have been used for the ANI study. (b) Dispersion curves were obtained from the two segments which are close to the tent indicated as 90 o IFD (ice flow direction) and 30 o IFD. The result from the linear array is also plotted.

6 Discussions

In this study, we investigate the use of noise data recorded by DAS, deployed on Rutford Ice Stream, West Antarctica, to obtain a high-resolution shear wave velocity profile of the firn. We compare CCs calculated over five days using a single DAS channel as a virtual source versus using three geophones (collocated or near collocated) as the virtual sources. A superior SNR is obtained with a geophone. The coherence of instrument noise over all the DAS channels degrades the cross-correlations, while introducing a geophone as a virtual source breaks down that coherence of the instrument noise.

Stable Rayleigh wave responses are retrieved from CCs between vertical component geophone data and horizontal component DAS data, as a result of the Rayleigh wave elliptical particle motion. We notice, however, that there are phase shifts introduced by: (1) the ellipticity produces a 90-degree phase shift between vertical and horizontal particle motions, (2) the difference between particle motion velocity and strain rate, and (3) the difference in instrument responses. However, these are not a problem for the dispersion analysis, as it only uses the slopes for calculating dispersion curves. We note that for studying waves other than Rayleigh waves, it might be beneficial to consider using the horizontal component parallel with the cable. We deliberately chose to use the vertical component to demonstrate the applicability of the hybrid instrument approach, because vertical component geophones are widely used for near-surface imaging applications

The noisy Rayleigh wave response from using a DAS channel as a virtual source is likely due to the instrument noise on DAS channels having a destructive impact on the CCs. Firstly, we can see clear horizontal bands in Figure 6a which are most dominant at t = 0, which therefore indicates that the instrument noise on each DAS channel is not independent. This is likely due to the nature of DAS measurement that senses the entire cable with a single interrogator unit, which results in such common mode noise (Lindsey et al., 2020), as shown in Figure S2.d. When a geophone is used as the virtual source, it breaks the coherency of this instrument noise. Additionally, we observe that the dominant seismic noise contributing to the seismic responses is transient in nature, therefore a large number of CCs derived from a DAS virtual source contain only instrument noise.

Based on our results we argue that deploying DAS together with conventional seismic instruments (hybrid instrumentation) would open more opportunities. This is consistent with previous studies, such as: combining seismometer and DAS for calculating receiver function and surface wave dispersion (Yu et al., 2019); converting strain to particle velocity or calibrating the conversion (Lindsey et al., 2020; Porritt et al., 2022; van den Ende & Ampuero, 2021), or to apply the H/V method between DAS and vertical component of a seismometer (Spica, Perton, et al., 2020).

Selective stacking is applied to improve CCs. Only 453 out of 3068 2-minute CCs panels are selected and stacked for shear wave inversions. With selective stacking, we eliminate a large chunk of data containing only instrument noise. The selected CCs contain mostly high-frequency signals from the snowmobile or transient low-frequency surface wave events. The snowmobile was used to approach the generator location in-line with the linear fibre optic cable array, 50 m away from the interrogator (Figure 11a), which produces a surface wave noise travelling along the fibre. The (suspected) crevassing generated surface wave signals are mostly from the shear margin of the ice stream (Figure S2), although not homogeneously distributed, they are generally in-line with the fibre optic cable.

The dispersion curves obtained from the passive and active datasets show strong agreement over the frequency range 10 to 50 Hz. While the hammer and plate source surveys produce energy down to 10 Hz, it is most stable above 15 Hz, which could provide a reliable S velocity profile down to ~60 m (Figure 10). The seismic noise interferometry extends the reliable measurement range down to 3 Hz, which enables an inversion over the entire column of the firn layer.

We did not observe clear ocean wave-related primary or secondary microseism noise as the dominant ambient noise on broadband seismometers from 0.01 to 1 Hz (Bensen et al., 2007). Previous studies with submarine DAS cables have recorded the microseism from 0.2 to 2 Hz (Sladen et al., 2019) and down to 0.5 Hz (Cheng et al., 2015; Spica, Nishida, et al., 2020). Some onshore studies also suggest the abundance of low-frequency noise with noise power spectrum analysis (Hudson et al., 2021; Lindsey et al., 2020a). It is, however, shown in our study that the DAS signals below 1 Hz are likely wind-related, which could due to shallow burial depth of the cable. It is also possible that the linear fibre is insensitive to microseism signals because of its propagation direction near perpendicular to the fibre.

The S-wave velocity profile obtained from this study fits well with the velocity profile which we inverted from a standard refraction P-wave experiment conducted in the BEAMISH project (Smith et al., 2021), assuming a Vp/Vs ratio of 1.95 (Smith et al., 2015) at depths of 0 to 80 m. Below 80 m the profiles from the methods diverge, with higher Vs at depths greater than 80 m from the surface wave inversion. This may suggest a decrease of the Vp/Vs ratio at depth, or an increase in azimuthal anisotropy. However, at these depths, the reliability of the standard refraction results decreases due to the data offset limitation of ~1 km. Also, spatial heterogeneity cannot be ruled out as the surveys are not collocated. Nevertheless, the shape and form of the inverted Vs profiles show good agreement with the refraction survey, with both methods showing a velocity-depth gradient change at around 12 m. This feature of the velocity profile indicates the depth of the critical density, marking the transition between the first two stages of the densification process (Herron & Langway, 1980). Above this depth, the dominant compaction mechanism is grain settling and packing and exhibits the highest densification rate. Below this transition progression to pore close-off occurs with a lower rate of densification. The velocity-depth gradients above and below this depth agree with this interpretation. This agreement between the methods, reproducing the velocity gradient transition at similar depths is significant. The standard refraction WHB method uses a double exponential fit to the travel-times (Kirchner & Bentley, 1979) which can force the presence of this gradient change when a simple polynomial fitting method may not. The results from noise interferometry and surface wave inversion, therefore, verify the assumption of the double exponential fitting step at this site and provide an independent and robust measure of this critical density transition in the firn profile.

With a triangular fibre optic array, we retrieve Rayleigh wave responses along 90° and 30° from the ice flow direction. We find a small difference between the two dispersion curves from 10 to 40 Hz. Considering uncertainties in the measurements, it qualitatively indicates no strong azimuthal anisotropy in the upper 80 m (the dominant sensitivity of this frequency band is the top 80 m (Figure 10b)). However, polarimetric radar measurements of Jordan et al. (2022) indicate azimuthal anisotropy at depths of 40 to 100 m across Rutford Ice Stream. Laterally, they find weaker anisotropy strength in the ice stream central (less deformation) than in the shear margin. Our measurements of the azimuthal variation of the Rayleigh wave-phase velocity contain uncertainties that may be due to lateral heterogeneity in the firn layer or instability of the cross-correlation functions. But within that uncertainty, our measurements are consistent with the Jordan et al. (2022) results and do not suggest high azimuthal anisotropy at the centre of the ice stream.

Our measurements of Vs complement those of Vp, without requiring additional S wave sources or 3-component sensors. The method uses DAS, collocated vertical component geophones, and natural seismic signals from crevasses and noise from snowmobiles, which means it could be convenient for the deployment and might be a feasible method for large-scale firn imaging. This may lead to an improved understanding of the mechanical properties of the firn and their variation. Although standard refraction methods can be adapted to derive a Vs profile, with S wave sources and 3 component instruments (King & Jarvis, 2007; Kirchner & Bentley, 1990), in general, only Vp profiles are measured. Efforts were made to reproduce the standard P-wave refraction survey method using diving P-waves from a hammer and plate source with DAS recording. However, inherent to the DAS method, a combination of the effects of gauge length and spatial averaging near the shot location, hinders the derivation of a high accuracy velocity profile. Nevertheless, our study suggests that DAS measurements and surface wave inversion have the potential to upscale for the investigation of firn properties over large areas.

Another potential benefit of the method presented here compared to the standard seismic refraction method is the capacity of the surface wave (passive or active) to image low-velocity layers (Zhang et al., 2007). The seismic refraction method would fail in the presence of low-velocity layers as no rays will undergo critical refraction at the top of it (base of the ice lens). This situation may arise where melt has occurred and refreezing produces ice lenses overlying lower velocity firn layers, as for example reported on Larsen C Ice Shelf (Ashmore et al., 2017).

Although the Vs profile in our study is inverted from noise CCs, we observe consistency between CC retrieved dispersion and active shot dispersion, which suggests the inversion methods would work with active seismic data as well. A source producing lower frequencies (e.g., explosives or weight drop) would allow greater depth penetration. Since Rayleigh wave signals are naturally acquired in conventional refraction surveys, revisiting these data with our method could provide an independent measurement of Vs and might yield new insights.

7 Conclusions

Applying noise interferometry to DAS data, we retrieved broadband (3 – 50 Hz) and stable CCs representing Rayleigh wave responses travelling along the DAS fibre. We show that the SNR improves when using a collocated geophone as the virtual source or selective stacking of only the best CCs (selection based on the tau-p domain). Noise sources are found to be transient including lower-frequency (2 – 10 Hz) surface wave signals from the shear margins of the ice stream, and high-frequency noise up to 80 Hz from a snowmobile. The Rayleigh wave dispersion curves are validated using active shot gathers.

Inverting the dispersion curves, we produce an S-wave velocity (Vs) profile of the firn layer, which resolves a ‘kink’ at 12 m depth, corresponding to the critical density where the mode of firn compaction changes. This model shows good agreement with a standard Vp refraction derived model. No significant azimuthal anisotropy is observed in the upper 80 m, using 10 to 40 Hz signal, which is consistent with previous studies that along the centre of the ice stream the top of the firn layer is not under strong horizontal deformation.

Our study demonstrates that the usage of surface waves, retrieved from DAS seismic noise interferometry, could complement the refraction Vp profiles, for studies of the firn layer. Since the acquisitions of DAS and seismic noise are simpler than geophone refraction surveying, these measurements have the potential to upscale to large areas of the ice sheets. This in turn might help decrease the uncertainty of mass balance estimation and palaeoclimate studies. Additionally, using surface waves instead of refraction waves will potentially allow investigation of the firn column where standard refraction methods fail in the presence of low velocity layers, such as have been observed on lower-latitude ice shelves. Finally, the methodology that we have developed can be easily applied to imaging the near surface in a host of other environmental applications where fibre optic cables can be deployed; examples include landslide monitoring, levee and embankment assessment, and sinkhole studies.

Acknowledgements

This work was funded by the UK’s Department for Business, Energy and Industrial Strategy through the DigiMon ACT CCS project (project number 299622), and the NERC

Collaborative Antarctic Science Scheme grant (grant number CASS-166). Fieldwork was undertaken as part of the BEAMISH Project (NERC AFI award numbers NE/G014159/1). We thank Silixa for the loan of an iDAS interrogator. Geophones were borrowed from the UK Geophysical Equipment Facility (GEF loan number 1111). Obspy (Krischer et al., 2015) is intensively used for data processing. The tau-p transform was performed with PyLops (Ravasi & Vasconcelos, 2020). Jelle Assink (KNMI) is thanked for useful discussion on the low-frequency signal in DAS and pointing out the weather data from ECMWF. Thomas Hudson, Sacha Lapins are thanked for useful discussions. Hanneke Paulssen is thanked for reading and commenting the manuscript. We thank Emma Smith and other two anonymous reviewers for their constructive comments.

Open Research

7 hours of continuous DAS data (decimated to 10 m channel distance and 100 Hz sampling rate), and continuous geophones data (3 collocated geophone, A000, R102, R104, vertical component) have been made available through Zenodo (Zhou et al. 2022), which could be used to reproduce the seismic noise interferometry and surface wave inversion for S wave velocity profile.

References

Ajo-Franklin, J. B., Dou, S., Lindsey, N. J., Monga, I., Tracy, C., Robertson, M., Rodriguez Tribaldos, V., Ulrich, C., Freifeld, B., Daley, T., & Li, X. (2019). Distributed Acoustic sensing Using Dark Fiber for Near-surface Characterization and Broadband seismic event Detection. *Scientific Reports*, *9*(1), 1328. https://doi.org/10.1038/s41598-018-36675-8

Alley, R. B. (1987). Firn densification by grain-boundary sliding: a first model. *Le Journal de Physique Colloques*, *48*(C1), C1-249-C1-256. https://doi.org/10.1051/jphyscol:1987135

Ashmore, D. W., Hubbard, B., Luckman, A., Kulessa, B., Bevan, S., Booth, A., Munneke, P. K., O'Leary, M., Sevestre, H., & Holland, P. R. (2017). Ice and firn heterogeneity within Larsen C Ice Shelf from borehole optical televiewing. *Journal of Geophysical Research: Earth Surface*, *122*(5), 1139–1153. https://doi.org/10.1002/2016JF004047

Bensen, G. D., Ritzwoller, M. H., Barmin, M. P., Levshin, A. L., Lin, F., Moschetti, M. P., Shapiro, N. M., & Yang, Y. (2007). Processing seismic ambient noise data to obtain reliable broad-band surface wave dispersion measurements. *Geophysical Journal International*, *169*(3), 1239–1260. https://doi.org/10.1111/j.1365-246X.2007.03374.x

Booth, A. D., Christoffersen, P., Schoonman, C., Clarke, A., Hubbard, B., Law, R., Doyle, S. H., Chudley, T. R., & Chalari, A. (2020). Distributed Acoustic Sensing of Seismic Properties in a Borehole Drilled on a Fast-Flowing Greenlandic Outlet Glacier. *Geophysical Research Letters*, *47*(13). https://doi.org/10.1029/2020GL088148

Brisbourne, A. M., Kendall, M., Kufner, S. K., Hudson, T. S., & Smith, A. M. (2021). Downhole distributed acoustic seismic profiling at Skytrain Ice Rise, West Antarctica. *Cryosphere*, *15*(7), 3443–3458. https://doi.org/10.5194/tc-15-3443-2021

Butcher, A., Hudson, T., Kendall, J., Kufner, S., Brisbourne, A., & Stork, A. (2021). Radon transform-based detection of microseismicity on DAS networks: A case study from Antarctica. *EAGE GeoTech 2021 - 1st EAGE Workshop on Induced Seismicity*. https://doi.org/10.3997/2214-4609.202131039

Butcher, A., Stork, A. L., Verdon, J. P., Kendall, J. M., Plenkers, K., Booth, F., Boneham, M., & Koe, A. (2021). Evaluating rock mass disturbance within open-pit excavations using seismic methods: A case study from the Hinkley Point C nuclear power station. *Journal of Rock Mechanics and Geotechnical Engineering*, *13*(3). https://doi.org/10.1016/j.jrmge.2020.12.001

Case, E., & Kingslake, J. (2022). Phase-sensitive radar as a tool for measuring firn compaction. *Journal of Glaciology*, *68*(267), 139–152. https://doi.org/10.1017/jog.2021.83

Chaput, J., Aster, R., Karplus, M., & Nakata, N. (2022). Ambient high-frequency seismic surface waves in the firn column of central west Antarctica. *Journal of Glaciology*, 1-14. https://doi.org/10.1017/jog.2021.135

Cheng, F., Chi, B., Lindsey, N. J., Dawe, T. C., & Ajo-Franklin, J. B. (2021). Utilizing distributed acoustic sensing and ocean bottom fiber optic cables for submarine structural characterization. *Scientific Reports*, *11*(1), 5613. https://doi.org/10.1038/s41598-021-84845-y

Cheng, F., Xia, J., Behm, M., Hu, Y., & Pang, J. (2019). Automated data selection in the Tau–p domain: Application to passive surface wave imaging. *Surveys in Geophysics*, 40(5), 1211-1228. https://doi.org/10.1007/s10712-019-09530-2

Cheng, F., Xia, J., Luo, Y., Xu, Z., Wang, L., Shen, C., Liu, R., Pan, Y., Mi, B., & Hu, Y. (2016). Multichannel analysis of passive surface waves based on crosscorrelations. GEOPHYSICS, 81(5), EN57–EN66. https://doi.org/10.1190/geo2015-0505.1

Cheng, F., Xia, J., Xu, Y., Xu, Z., & Pan, Y. (2015). A new passive seismic method based on seismic interferometry and multichannel analysis of surface waves. *Journal of Applied Geophysics*, *117*, 126–135. https://doi.org/10.1016/j.jappgeo.2015.04.005

Correa, J., Freifeld, B. M., Revzner, R., Wood, T., Tertyshnikov, K., & Bona, A. (2018). Continuous DAS VSP monitoring using surface orbital vibrators: Field trials for optimal configuration at the CO2CRC Otway Project. *80th EAGE Conference and Exhibition 2018 Workshop Programme*, cp--00040. https://doi.org/10.3997/2214-4609.201801917

Craig, H., Horibe, Y., & Sowers, T. (1988). Gravitational Separation of Gases and Isotopes in Polar Ice Caps. *Science*, *242*(4886), 1675–1678. https://doi.org/10.1126/science.242.4886.1675

Cuffey, K. M., & Paterson, W. S. B. (2010). Physics of Glaciers, Fourth Edition. In *The Physics of Glaciers*.

Diebold, J. B., & Stoffa, P. L. (1981). The traveltime equation, tau-p mapping, and inversion of common midpoint data. *Geophysics*, *46*(3). https://doi.org/10.1190/1.1441196

Dou, S., Lindsey, N., Wagner, A. M., Daley, T. M., Freifeld, B., Robertson, M., Peterson, J., Ulrich, C., Martin, E. R., & Ajo-Franklin, J. B. (2017). Distributed Acoustic Sensing for Seismic Monitoring of The Near Surface: A Traffic-Noise Interferometry Case Study. *Scientific Reports*, *7*(1), 11620. https://doi.org/10.1038/s41598-017-11986-4

European Centre for Medium-Range Weather Forecasts (2017). ERA5 Reanalysis, https://doi.org/10.5065/D6X34W69, Research Data Archive at the National Center for Atmospheric Research, Computational and Information Systems Laboratory, Boulder, Colo. (Updated monthly.) Accessed 07 Jun 2022.

Harland, S. R., Kendall, J.-M. ., Stuart, G. W., Lloyd, G. E., Baird, A. F., Smith, A. M., Pritchard, H. D., & Brisbourne, A. M. (2013). Deformation in Rutford Ice Stream, West Antarctica: measuring shear-wave anisotropy from icequakes. Annals of Glaciology, 54(64), 105–114. https://doi.org/10.3189/2013AoG64A033

He, X., Xie, S., Liu, F., Cao, S., Gu, L., Zheng, X., & Zhang, M. (2017). Multi-event waveform-retrieved distributed optical fiber acoustic sensor using dual-pulse heterodyne phase-sensitive OTDR. *Optics Letters*, *42*(3), 442. https://doi.org/10.1364/OL.42.000442

Herrmann, R. B. (2013). Computer programs in seismology: An evolving tool for instruction and research. *Seismological Research Letters*, *84*(6). https://doi.org/10.1785/0220110096

Herron, M. M., & Langway, C. C. (1980). Firn densification: an empirical model. *Journal of Glaciology*, *25*(93). https://doi.org/10.1017/S0022143000015239

Hollmann, H., Treverrow, A., Peters, L. E., Reading, A. M., & Kulessa, B. (2021). Seismic observations of a complex firn structure across the Amery Ice Shelf, East Antarctica. *Journal of Glaciology*, *67*(265), 777–787. https://doi.org/10.1017/jog.2021.21

Hudson, T. S., Baird, A. F., Kendall, J. M., Kufner, S. K., Brisbourne, A. M., Smith, A. M., Butcher, A., Chalari, A., & Clarke, A. (2021). Distributed Acoustic Sensing (DAS) for Natural Microseismicity Studies: A Case Study From Antarctica. *Journal of Geophysical Research: Solid Earth*, *126*(7). https://doi.org/10.1029/2020JB021493

Ide, S., Araki, E., & Matsumoto, H. (2021). Very broadband strain-rate measurements along a submarine fiber-optic cable off Cape Muroto, Nankai subduction zone, Japan. *Earth, Planets and Space*, *73*(1), 63. https://doi.org/10.1186/s40623-021-01385-5

Jordan, T. M., Martín, C., Brisbourne, A. M., Schroeder, D. M., & Smith, A. M. (2022). Radar Characterization of Ice Crystal Orientation Fabric and Anisotropic Viscosity Within an Antarctic Ice Stream. *Journal of Geophysical Research: Earth Surface*, *127*(6). https://doi.org/10.1029/2022jf006673

Jordan, T. M., Schroeder, D. M., Elsworth, C. W., & Siegfried, M. R. (2020). Estimation of ice fabric within Whillans Ice Stream using polarimetric phase-sensitive radar sounding. *Annals of Glaciology*, *61*(81), 74–83. https://doi.org/10.1017/aog.2020.6

King, E. C., & Jarvis, E. P. (2007). Use of Shear Waves to Measure Poisson's Ratio in Polar Firn. *Journal of Environmental and Engineering Geophysics*, *12*(1), 15–21. https://doi.org/10.2113/JEEG12.1.15

Kirchner, J. F., & Bentley, C. R. (1979). Seismic Short-Refraction Studies on the Ross Ice Shelf, Antarctica. *Journal of Glaciology*, *24*(90), 313–319. https://doi.org/10.3189/S0022143000014830

Kirchner, J. F., & Bentley, C. R. (1990). *RIGGS III: Seismic Short-Refraction Studies Using an Analytical Curve-Fitting Technique* (pp. 109–126). https://doi.org/10.1029/AR042p0109

Krischer, L., Megies, T., Barsch, R., Beyreuther, M., Lecocq, T., Caudron, C., & Wassermann, J. (2015). ObsPy: a bridge for seismology into the scientific Python ecosystem. *Computational Science & Discovery*, *8*(1), 014003. https://doi.org/10.1088/1749-4699/8/1/014003

Kufner, S., Brisbourne, A. M., Smith, A. M., Hudson, T. S., Murray, T., Schlegel, R., Kendall, J. M., Anandakrishnan, S., & Lee, I. (2021). Not all Icequakes are Created Equal: Basal Icequakes Suggest Diverse Bed Deformation Mechanisms at Rutford Ice Stream, West Antarctica. *Journal of Geophysical Research: Earth Surface*, *126*(3). https://doi.org/10.1029/2020JF006001

Lellouch, A., Yuan, S., Spica, Z., Biondi, B., & Ellsworth, W. L. (2019). Seismic Velocity Estimation Using Passive Downhole Distributed Acoustic Sensing Records: Examples

From the San Andreas Fault Observatory at Depth. *Journal of Geophysical Research: Solid Earth*, *124*(7), 6931–6948. https://doi.org/10.1029/2019JB017533

Lindner, F., Laske, G., Walter, F., & Doran, A. K. (2019). Crevasse-induced Rayleigh-wave azimuthal anisotropy on Glacier de la Plaine Morte, Switzerland. *Annals of Glaciology*, *60*(79), 96–111. https://doi.org/10.1017/aog.2018.25

Lindsey, N. J., Rademacher, H., & Ajo-Franklin, J. B. (2020). On the Broadband Instrument Response of Fiber-Optic DAS Arrays. *Journal of Geophysical Research: Solid Earth*, *125*(2), 1–16. https://doi.org/10.1029/2019JB018145

Lior, I., Mercerat, E. D., Rivet, D., Sladen, A., & Ampuero, J.-P. (2021). *Imaging an Underwater Basin and its Resonance Modes using Optical Fiber Distributed Acoustic Sensing*. https://doi.org/https://doi.org/10.31223/X5XK8P

Lior, I., Sladen, A., Rivet, D., Ampuero, J., Hello, Y., Becerril, C., Martins, H. F., Lamare, P., Jestin, C., Tsagkli, S., & Markou, C. (2021). On the Detection Capabilities of Underwater Distributed Acoustic Sensing. *Journal of Geophysical Research: Solid Earth*, *126*(3), 1–20. https://doi.org/10.1029/2020JB020925

Luu, K. (2021). *disba: Numba-accelerated computation of surface wave dispersion*. https://doi.org/https://doi.org/10.5281/zenodo.3987395

Mateeva, A., Lopez, J., Chalenski, D., Tatanova, M., Zwartjes, P., Yang, Z., Bakku, S., Vos, K. de, & Potters, H. (2017). 4D das VSP as a tool for frequent seismic monitoring in deep water. *Leading Edge*, *36*(12), 995–1000. https://doi.org/10.1190/tle36120995.1

Morris, E. M., Mulvaney, R., Arthern, R. J., Davies, D., Gurney, R. J., Lambert, P., De Rydt, J., Smith, A. M., Tuckwell, R. J., & Winstrup, M. (2017). Snow Densification and Recent Accumulation Along the iSTAR Traverse, Pine Island Glacier, Antarctica. *Journal of*

Geophysical Research: Earth Surface, *122*(12), 2284–2301. https://doi.org/10.1002/2017jf004357

Murray, T., Smith, A. M., King, M. A., & Weedon, G. P. (2007). Ice flow modulated by tides at up to annual periods at Rutford Ice Stream, West Antarctica. *Geophysical Research Letters*, *34*(18), L18503. https://doi.org/10.1029/2007GL031207

Olivier, G., Brenguier, F., Campillo, M., Lynch, R., & Roux, P. (2015). Body-wave reconstruction from ambient seismic noise correlations in an underground mine. *GEOPHYSICS*, *80*(3). https://doi.org/10.1190/geo2014-0299.1

Park, C. B., Miller, R. D., & Xia, J. (1999). Multichannel analysis of surface waves. GEOPHYSICS, 64(3), 800–808. https://doi.org/10.1190/1.1444590

Park, C., Miller, R., Laflen, D., Bennett, B., Ivanov, J., Neb, C., & Huggins, R. (2004). Imaging dispersion curves of passive surface waves. 2004 SEG Annual Meeting.

Peters, L. E., Anandakrishnan, S., Alley, R. B., Winberry, J. P., Voigt, D. E., Smith, A. M., & Morse, D. L. (2006). Subglacial sediments as a control on the onset and location of two Siple Coast ice streams, West Antarctica. Journal of Geophysical Research, 111(B1). https://doi.org/10.1029/2005jb003766

Porritt, R., Abbott, R., & Poppeliers, C. (2022). Quantitative assessment of Distributed Acoustic Sensing at the Source Physics Experiment, Phase II. https://doi.org/10.2172/1855336

Ravasi, M., & Vasconcelos, I. (2020). PyLops—A linear-operator Python library for scalable algebra and optimization. *SoftwareX*, *11*, 100361. https://doi.org/10.1016/j.softx.2019.100361

Riverman, K. L., Alley, R. B., Anandakrishnan, S., Christianson, K., Holschuh, N. D., Medley, B., Muto, A., & Peters, L. E. (2019). Enhanced Firn Densification in High-Accumulation

Shear Margins of the NE Greenland Ice Stream. *Journal of Geophysical Research: Earth Surface*, *124*(2), 365–382. https://doi.org/10.1029/2017JF004604

Rodríguez Tribaldos, V., & Ajo-Franklin, J. B. (2021). Aquifer Monitoring Using Ambient Seismic Noise Recorded With Distributed Acoustic Sensing (DAS) Deployed on Dark Fiber. *Journal of Geophysical Research: Solid Earth*, *126*(4), 1–20. https://doi.org/10.1029/2020jb021004

Rodríguez Tribaldos, V., Ajo-Franklin, J., Dou, S., Lindsey, N., Ulrich, C., Robertson, M., Freifeld, B., Daley, T., Monga, I., & Tracy, C. (2019). *Surface Wave Imaging using Distributed Acoustic Sensing Deployed on Dark Fiber: Moving Beyond High Frequency Noise*. https://doi.org/10.31223/OSF.IO/JB2NA

Rücker, C., Günther, T., & Wagner, F. M. (2017). pyGIMLi: An open-source library for modelling and inversion in geophysics. *Computers & Geosciences*, *109*, 106–123. https://doi.org/10.1016/j.cageo.2017.07.011

Schimmel, M., & Paulssen, H. (1997). Noise reduction and detection of weak, coherent signals through phase-weighted stacks. *Geophysical Journal International*, *130*(2), 497–505. https://doi.org/10.1111/j.1365-246X.1997.tb05664.x

Schimmel, M., Stutzmann, E., & Gallart, J. (2011). Using instantaneous phase coherence for signal extraction from ambient noise data at a local to a global scale. *Geophysical Journal International*, *184*(1), 494–506. https://doi.org/10.1111/j.1365-246X.2010.04861.x

Schlegel, R., Diez, A., Löwe, H., Mayer, C., Lambrecht, A., Freitag, J., Miller, H., Hofstede, C., & Eisen, O. (2019). Comparison of elastic moduli from seismic diving-wave and ice-core microstructure analysis in Antarctic polar firn. *Annals of Glaciology*, *60*(79), 220–230. https://doi.org/10.1017/aog.2019.10

Sergeant, A., Chmiel, M., Lindner, F., Walter, F., Roux, P., Chaput, J., Gimbert, F., & Mordret, A. (2020). On the Green's function emergence from interferometry of seismic wave fields generated in high-melt glaciers: implications for passive imaging and monitoring. *The Cryosphere*, *14*(3), 1139–1171. https://doi.org/10.5194/tc-14-1139-2020

Shapiro, N. M., & Campillo, M. (2004). Emergence of broadband Rayleigh waves from correlations of the ambient seismic noise. *Geophysical Research Letters*, *31*(7), 8–11. https://doi.org/10.1029/2004GL019491

Shapiro, N. M., Campillo, M., Stehly, L., & Ritzwoller, M. H. (2005). High-resolution surface-wave tomography from ambient seismic noise. *Science*, *307*(5715), 1615–1618.

Shepherd, A., Ivins, E. R., Geruo, A., Barletta, V. R., Bentley, M. J., Bettadpur, S., Briggs, K. H., Bromwich, D. H., Forsberg, R., Galin, N., Horwath, M., Jacobs, S., Joughin, I., King, M. A., Lenaerts, J. T. M., Li, J., Ligtenberg, S. R. M., Luckman, A., Luthcke, S. B., … Zwally, H. J. (2012). A reconciled estimate of ice-sheet mass balance. *Science*, *338*(6111). https://doi.org/10.1126/science.1228102

Slichter, L. B. (1932). The Theory of the Interpretation of Seismic Travel-Time Curves in Horizontal Structures. *Physics*, *3*(6), 273–295. https://doi.org/10.1063/1.1745133

Smith, A. M. (1997). Variations in basal conditions on Rutford Ice Stream, West Antarctica. *Journal of Glaciology*, *43*(144), 245–255. https://doi.org/10.3189/S0022143000003191

Smith, A. M., Anker, P. G. D., Nicholls, K. W., Makinson, K., Murray, T., Rios-Costas, S., Brisbourne, A. M., Hodgson, D. A., Schlegel, R., & Anandakrishnan, S. (2021). Ice stream subglacial access for ice-sheet history and fast ice flow: the BEAMISH Project on Rutford Ice Stream, West Antarctica and initial results on basal conditions. *Annals of Glaciology*, *62*(85–86), 203–211. https://doi.org/10.1017/aog.2020.82

Smith, E. C., Baird, A. F., Kendall, J. M., Martín, C., White, R. S., Brisbourne, A. M., & Smith, A. M. (2017). Ice fabric in an Antarctic ice stream interpreted from seismic anisotropy. *Geophysical Research Letters*, *44*(8), 3710–3718. https://doi.org/10.1002/2016GL072093

Smith, E. C., Smith, A. M., White, R. S., Brisbourne, A. M., & Pritchard, H. D. (2015). Mapping the ice-bed interface characteristics of Rutford Ice Stream, West Antarctica, using microseismicity. *Journal of Geophysical Research: Earth Surface*, *120*(9), 1881–1894. https://doi.org/10.1002/2015JF003587

Snieder, R., & Larose, E. (2013). Extracting Earth's Elastic Wave Response from Noise Measurements. *Annual Review of Earth and Planetary Sciences*, *41*(1), 183–206. https://doi.org/10.1146/annurev-earth-050212-123936

Spica, Z. J., Nishida, K., Akuhara, T., Pétrélis, F., Shinohara, M., & Yamada, T. (2020). Marine Sediment Characterized by Ocean-Bottom Fiber-Optic Seismology. *Geophysical Research Letters*, *47*(16), e2020GL088360. https://doi.org/10.1029/2020GL088360

Spica, Z. J., Perton, M., Martin, E. R., Beroza, G. C., & Biondi, B. (2020). Urban Seismic Site Characterization by Fiber-Optic Seismology. *Journal of Geophysical Research: Solid Earth*, *125*(3), 1–14. https://doi.org/10.1029/2019JB018656

van den Broeke, M. (2005). Strong surface melting preceded collapse of Antarctic Peninsula ice shelf. *Geophysical Research Letters*, *32*(12), 1–4. https://doi.org/10.1029/2005GL023247

van den Broeke, M. (2008). Depth and Density of the Antarctic Firn Layer. *Arctic, Antarctic, and Alpine Research*, *40*(2), 432–438. https://doi.org/10.1657/1523-0430(07-021)

van den Ende, M. P. A., & Ampuero, J. P. (2021). Evaluating seismic beamforming capabilities of distributed acoustic sensing arrays. *Solid Earth*, *12*(4), 915–934. https://doi.org/10.5194/se-12-915-2021

Vidal, C. A., Draganov, D., van der Neut, J., Drijkoningen, G., & Wapenaar, K. (2014). Retrieval of reflections from ambient noise using illumination diagnosis. *Geophysical Journal International*, *198*(3), 1572–1584. https://doi.org/10.1093/gji/ggu164

Walter, F., Gräff, D., Lindner, F., Paitz, P., Köpfli, M., Chmiel, M., & Fichtner, A. (2020). Distributed acoustic sensing of microseismic sources and wave propagation in glaciated terrain. *Nature Communications*, *11*(1), 2436. https://doi.org/10.1038/s41467-020-15824-6

Walter, F., Roux, P., Roeoesli, C., Lecointre, A., Kilb, D., & Roux, P. F. (2015). Using glacier seismicity for phase velocity measurements and Green's function retrieval. *Geophysical Journal International*, *201*(3). https://doi.org/10.1093/gji/ggv069

Williams, E. F., Fernández-Ruiz, M. R., Magalhaes, R., Vanthillo, R., Zhan, Z., González-Herráez, M., & Martins, H. F. (2019). Distributed sensing of microseisms and teleseisms with submarine dark fibers. *Nature Communications*, *10*(1), 1–11. https://doi.org/10.1038/s41467-019-13262-7

Xia, J., Xu, Y., & Miller, R. D. (2007). Generating an Image of Dispersive Energy by Frequency Decomposition and Slant Stacking. Pure and Applied Geophysics, 164(5), 941–956. https://doi.org/10.1007/s00024-007-0204-9

Xia, J., Miller, R. D., & Park, C. B. (1999). Estimation of near-surface shear-wave velocity by inversion of Rayleigh waves. *GEOPHYSICS*, *64*(3), 691–700. https://doi.org/10.1190/1.1444578

Yu, C., Zhan, Z., Lindsey, N. J., Ajo-Franklin, J. B., & Robertson, M. (2019). The Potential of DAS in Teleseismic Studies: Insights From the Goldstone Experiment. *Geophysical Research Letters*, *46*(3), 1320–1328. https://doi.org/10.1029/2018GL081195

Yudistira, T., Paulssen, H., & Trampert, J. (2017). The crustal structure beneath The Netherlands derived from ambient seismic noise. In *Tectonophysics* (Vol. 721, Issue 77). https://doi.org/10.1016/j.tecto.2017.09.025

Zhang, X., Paulssen, H., Lebedev, S., & Meier, T. (2007). Surface wave tomography of the Gulf of California. *Geophysical Research Letters*, *34*(15). https://doi.org/10.1029/2007GL030631

Zhou, W., Butcher, A., Brisbourne, A., Kufner, S., Kendall, J. M., & Stork, A. (2022). Seismic noise interferometry and Distributed Acoustic Sensing (DAS): measuring the firn layer S-velocity structure on Rutford Ice Stream, Antarctica (v.0.0.1) [Data set]. Zenodo. https://doi.org/10.5281/zenodo.7064405

Zhou, W., & Paulssen, H. (2020). Compaction of the Groningen gas reservoir investigated with train noise. *Geophysical Journal International*, *223*(2), 1327–1337. https://doi.org/10.1093/gji/ggaa364